Journal of Marine Science and Technology

Volume 22 | Issue 3 Article 10

THE DEVELOPMENT OF A COST-EFFECTIVE AND OPTIMIZED DP-SPIV SYSTEM FOR FLUID TURBULENCE RESEARCHES

Yu-Chi Chang
Department of Systems Engineering and Naval Architecture, National Taiwan Ocean University, Keelung, Taiwan, R.O.C

Yi-Hung Chang
Department of Systems Engineering and Naval Architecture, National Taiwan Ocean University, Keelung, Taiwan, R.O.C.

Yaw-Huei Lee
Department of Systems Engineering and Naval Architecture, National Taiwan Ocean University, Keelung, Taiwan, R.O.C.

Yi-Chih Chow
Department of Systems Engineering and Naval Architecture, National Taiwan Ocean University, Keelung, Taiwan, R.O.C., ycchow@ntou.edu.tw

Journal of Marine Science and Technology, Vol. 22, No. 3, pp. 362-371 (2014)
DOI: 10.6119/JMST-012-1207-3

THE DEVELOPMENT OF A COST-EFFECTIVE AND OPTIMIZED DP-SPIV SYSTEM FOR FLUID TURBULENCE RESEARCHES

Yu-Chi Chang, Yi-Hung Chang, Yaw-Huei Lee, and Yi-Chih Chow

Key words: turbulence modeling, DP-SPIV, birefringent optics, continuity equation, Scheimpflug condition, system optimization.

ABSTRACT

Turbulent flows and issues of turbulence modeling have long been intriguing and important in fluid researches and practices. The mean or instantaneous velocity gradient tensors with six independent components, or other tensorial variables involving gradients, play a key role in turbulence dynamics and models. The advancement of the knowledge of these parameters relies on measurement systems built on sophisticated flow diagnostic techniques that enable both detailed and complete measurements. However, such systems seem inevitably complicated to operate and costly to build and maintain. Therefore, we develop and optimize a dual-plane stereoscopic particle image velocimetry (DP-SPIV) system that is much more cost-effective than the conventional setup while maintain its full functionalities. Conventional DP-SPIV systems require two double-pulse lasers, four PIV cameras, and complex optical arrangements including a refractive-index-matched prism that need delicate calibrations. We reduce the numbers of double-pulse laser, camera, and prism to one, three, and zero, respectively, with applications of birefringent optics, the continuity equation, and Scheimpflug condition. The complexities of optical arrangements, namely the polarizations and parallelism of the two light sheets and the prism, are also significantly reduced. The optimized system results in a cost-down of nearly one half and reduction of setup time to almost one order of magnitude shorter.

I. INTRODUCTION

The fluid flows encountered in human's daily lives are mostly turbulent. In order to predict, control, and make use of turbulent flows to the good of mankind, it is pivotal to develop an accurate numerical model to quantitatively describe turbulence. The most accurate turbulence modeling is the so-called DNS (Direct Numerical Simulation), meaning that the Navier-Stokes equations are solved directly without imposing any models. However, DNS needs enormous amount of computing resources and can only achieve computations of low-Reynolds-number flows of simple geometries [12], i.e., not a practical tool to deal with common turbulent flows. Methodologically, RANS (Reynolds-Averaged Navier-Stokes equation solver) and LES (Large Eddy Simulation) can be regarded as the other two types of turbulence modeling. Thanks to the modeling efforts, RANS and LES use much less computing power than DNS does. However, the accuracy and performance of the modeling becomes the major issue of solving turbulent flows.

In the model development of RANS, there have been three main types of modeling: one-equation model, two-equation model (e.g., $k-\varepsilon$ model [7], $k-\omega$ model [17]), and Reynolds stress model (RSM) [6]. The key objective of RANS modeling is to model Reynolds stresses. Using $k-\varepsilon$ model as an example, its k equation:

$$\frac{Dk}{Dt}=\nabla\cdot\left(\frac{\nu_T}{\sigma_k}\nabla k\right)-\overline{u_i'u_j'}\frac{\partial\overline{u}_i}{\partial x_j}-\nu\overline{\frac{\partial u_i'}{\partial x_j}\frac{\partial u_i'}{\partial x_j}},\ k=\frac{1}{2}\left(\overline{u_i'u_i'}\right) \quad (1)$$

where k denotes the turbulent kinetic energy, ν_T denotes the eddy viscosity, σ_k is a model constant, u_i and u_j (i, j = 1, 2, 3) denote the components of the fluid velocity, ν denotes the kinetic viscosity of fluid, and the overbar denotes the averaging operation. And $u_i=\overline{u}_i+u_i'$. Reynolds stresses are linked to k and velocity gradients through Boussinesq hypothesis [4]:

$$\overline{u_i'u_j'}=\frac{2}{3}k\delta_{ij}-\nu_T\left(\frac{\partial\overline{u}_i}{\partial x_j}+\frac{\partial\overline{u}_j}{\partial x_i}\right) \quad (2)$$

where δ_{ij} denotes Kronecker delta. For LES [15], SubGrid-

Paper submitted 08/20/12; revised 11/01/12; accepted 12/07/12. Author for correspondence: Yi-Chih Chow (e-mail: ycchow@ntou.edu.tw).
Department of Systems Engineering and Naval Architecture, National Taiwan Ocean University, Keelung, Taiwan, R.O.C.

Scale (SGS) stresses are modeled based on Boussinesq hypothesis as well, i.e., closely related with velocity gradients as well. Eq. (3) shows the Reynolds stress transport equation

$$\frac{\partial}{\partial t}\overline{u_i' u_j'} + \overline{u}_k \frac{\partial}{\partial x_k}\overline{u_i' u_j'} = -\frac{\partial}{\partial x_k}\overline{u_i' u_j' u_k'} + \nu \frac{\partial^2}{\partial x_k \partial x_k}\overline{u_i' u_j'}$$

$$-\left(\overline{u_i' u_k'}\frac{\partial \overline{u}_j}{\partial x_k} + \overline{u_j' u_k'}\frac{\partial \overline{u}_i}{\partial x_k}\right) - \frac{1}{\rho}\overline{u_i' \frac{\partial p'}{\partial x_j}} + \overline{u_j' \frac{\partial p'}{\partial x_i}} - 2\nu \overline{\frac{\partial u_i'}{\partial x_k}\frac{\partial u_j'}{\partial x_k}} \qquad (3)$$

where p' denotes the fluctuating pressure. From Eq. (3), it is evident that almost all of the terms are concerned with (mean or fluctuating) velocity gradients. It can be said that a measurement system capable of resolving full velocity gradients is quite needed for advancing turbulence models.

PIV (Particle Image Velocimetry) is a powerful, non-intrusive flow measurement technique. Its working principle is to image flow tracers (particles) and analyze these particle images to retrieve flow velocity information [11]. PIV as a "multi-point" measurement technique has surpassed the previous "single-point" ones such as pitot tube, hot-wire anemometry, and LDV (Laser Doppler Velocimetry). According to the dimension (D) of measurement and the velocity components (C) resolved, PIV can be characterized as 2D-2C PIV, 2D-3C PIV, and 3D-3C PIV. The base-line, 2D-2C PIV mainly consisting of one PIV camera and one double-pulse laser, i.e., the minimum requirement of equipments for a PIV system, can resolve variables associated with only two velocity components and gradients in only two directions. In order to obtain the third component of velocity, SPIV (Stereoscopic PIV, [10]) as the major type of 2D-3C PIV has been developed using two PIV cameras viewing the same area of measurement at an angle like human's eyes to further resolve the out-of-plane velocity component (in depth). On the high end of PIV systems, 3D-3C PIV (e.g., Holographic PIV [18], Tomographic PIV [1], and Defocusing PIV [9]) is capable of resolving tensorial variables in full. The obvious drawbacks of 3D-3C PIV, however, are system complexities, precision requirements of optics, and the cost and setup time associated with such difficulties.

To circumvent the issues with 3D-3C PIV, DP-SPIV (Dual-plane stereoscopic PIV) as an intermediate between 2D-3C PIV and 3D-3C PIV has been developed. As shown in Fig. 1, the conventional DP-SPIV system mainly consists of two double-pulse lasers and four PIV cameras. These two lasers and associated optical components generate two parallel, mutually orthogonally polarized light sheets. Then four PIV cameras arranged as two SPIV camera sets with polarizing beam splitters acquire images from different light sheets. Therefore, data sets of full velocity on two closely-spaced planes can be obtained and, as a result, complete tensorial variables on a plane can be resolved. It should be noted that the conventional DP-SPIV system achieves the desired resolving functionality at the expense of involving still significant amount of components and a resulting complex structure. In addition, a prism with refractive index matched with that of the fluid (e.g., water) is traditionally used in this system to reduce optical distortions caused by the significant difference in refractive indexes of the fluid and the media around the cameras (e.g., the air). In other words, the use of a prism results in extra complications to the system. It is therefore the goal of this paper to optimize this system and develop a cost-effective measure tool for fluid turbulence researches.

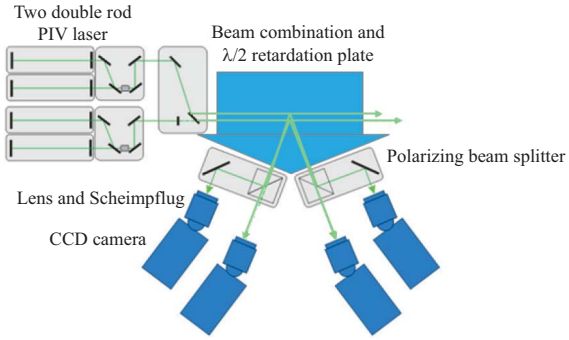

Fig. 1. Conventional DP-PIV System (adapted from LaVision's business presentation).

II. OPTIMIZATION OF DP-SPIV

We start by investigating three aspects of a DP-SPIV system: (1) the dual-plane light sheet generation; (2) the four-camera setup (two stereoscopic camera pairs); (3) the usage of a refractive-index-matched prism.

1. Dual-Plane Light Sheet Generation

Instead of using two lasers, it is possible to make two light sheets out of one laser beam. For example, Tanahashi *et al.* [16] used an optical arrangement to split one laser beam into two parallel, orthogonally polarized beams for light sheet generation. However, their optical setup is quite complicated mainly due to the requirement of parallelism of two closely-spaced light sheets. In the system presented in this paper, we use a single "birefringent" lens to achieve the same goal with a drastically simplified configuration. As shown in Fig. 2(a), birefringent optics can split one laser beam into two parallel, mutually polarization-perpendicular e-ray and o-ray, with one single crystal (lens). The specifications and manufacture precisions of the birefringent lens used in this paper are listed in Table 1. Because of its high manufacture precisions, the parallelism of, the desired polarizations of, and the distance (walk-off) between the beams split by a birefringent lens can be easily achieved. Fig. 2(b) shows a sample image of a lab test for generation of two light sheets through the birefringent lens. Therefore, by using a single birefringent lens, the number of laser used is reduced to 1 and the complexity of the optical arrangement in the DP-SPIV system can be minimized.

Table 1. Specifications of the birefringent lens used.

Specification	Size
Material	Calcite-Grade A
Dimension	5.0 mm * 5.0 mm
Length	10.0 mm
SQ	20/10
Transmitted Wavefront	<lambda/4@633 nm
Beam Deviation	<=3 arcmin
Bevel	0.3 mm@45 deg
CA	>=85%
Walk-off	1.0 mm at 532 nm

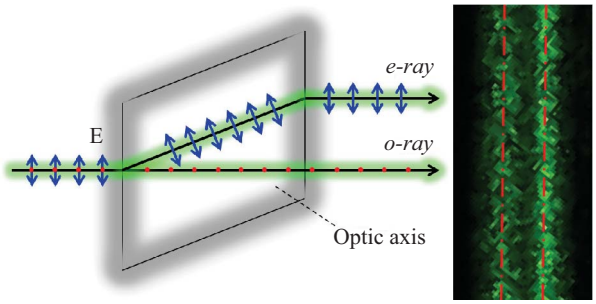

Fig. 2. (a) Birefringent optics [3], and (b) a sample image of two parallel light sheets generated using a birefringent lens.

2. Four-Camera Setup Reduction

The conventional DP-SPIV system uses two sets of camera pair to form a stereoscopic view for each plane illuminated by a laser light sheet. By doing so, the three components (u, v, w) of the velocity vectors distributed on each plane can be resolved. Further using finite difference schemes, all velocity gradients $\partial u/\partial x$, $\partial v/\partial x$, $\partial w/\partial x$, $\partial u/\partial y$, $\partial v/\partial y$, $\partial w/\partial y$, $\partial u/\partial z$, $\partial v/\partial z$, and $\partial w/\partial z$ can be obtained. However, the continuity equation

$$\frac{\partial u}{\partial x}+\frac{\partial v}{\partial y}+\frac{\partial w}{\partial z}=0 \tag{4}$$

shows the dependence between the velocity vectors of different planes, i.e., $\partial w/\partial z$. It implies that by applying the continuity equation, one SPIV camera set can be reduced to 2D-2C PIV, i.e., requiring only one camera. Bharathram *et al*. [2] and Saikrishnan *et al*. [13] implemented this idea and constructed a successful DP-SPIV system using three cameras. In this study, we adopt this kind of camera arrangement and also successfully reduce the number of cameras from 4 to 3.

3. Scheimpflug Condition and Prism

In stereoscopic photography, images suffer varying magnification across their fields of view. As a result, SPIV images need to be calibrated using setup as shown in Fig. 3(a), where a calibration target is imaged by two cameras in the stereoscopic

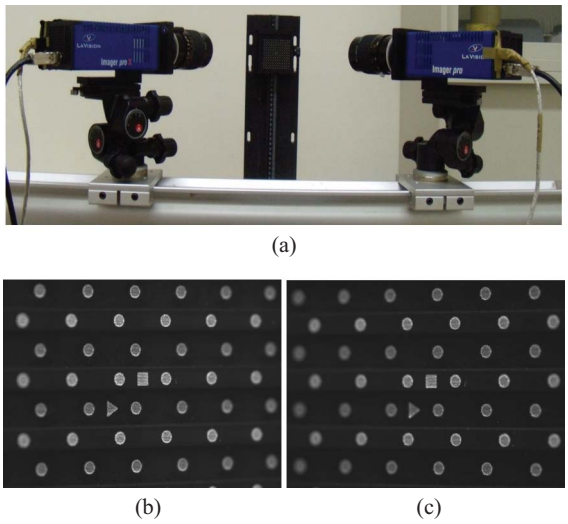

Fig. 3. (a) SPIV calibration setup, (b) a sample calibration image from the left camera, and (c) a sample calibration image from the right camera.

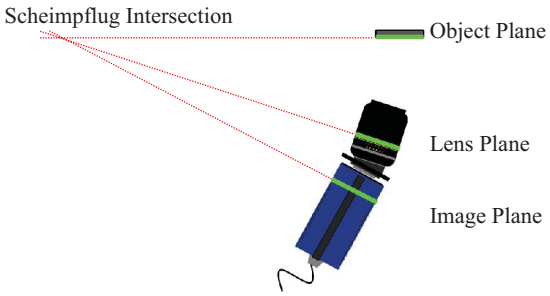

Fig. 4. Schematic of Scheimpflug condition. The green bars denote the laser pointers used to aid reaching Scheimpflug condition.

configuration. As shown in Figs. 3(b) and 3(c), stereoscopic images are not uniformly focused if Scheimpflug condition [14] is not satisfied. Scheimpflug condition means that the object plane, the lens plane and the image plane intersect at the same line, as illustrated in Fig. 4. Therefore, SPIV setup adopts certain adjustable connection between the camera and the lens in order to realize Scheimpflug condition, as illustrated in Fig. 4. Scheimpflug condition must be satisfied in order to make images in focus, and thus becomes part of the calibration procedures for SPIV. Here we use LaVison's DaVis 7 software [8] to compute the transformation and fitting for calibration. The calibration can be considered done when the calibration error calculated by the software is below 2 pixels [8].

As aforementioned, a prism is usually used to reduce optical distortions caused by the difference in refractive indexes of the fluid and the media around the cameras. The usage of a prism, however, results in two major disadvantages. First, the prism is usually made like a container to be filled with fluid having the same refractive index as that of the object fluid. Securely and water-tightly attaching the prism to the side

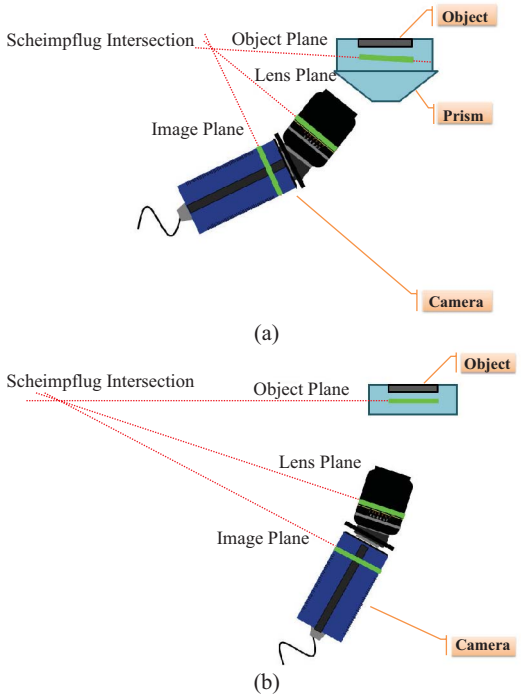

Fig. 5. Schematic of test cases: (a) with a prism, and (b) without a prism.

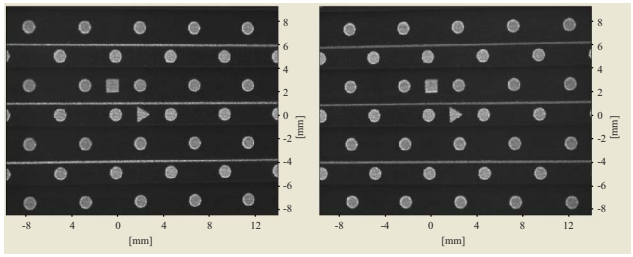

Fig. 6. Clear images obtained in a full SPIV calibration without using a prism.

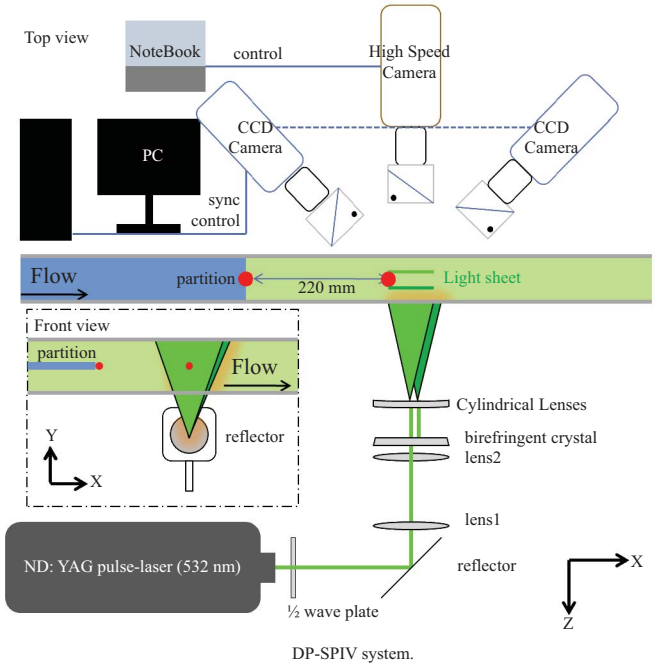

Fig. 7. Schematic of the optimized DP-SPIV system.

window of the experimental facility becomes problematic. Second, if the viewing angles of cameras change for a reason, the shape of the prism needs to change accordingly, i.e., a new prism needs to be made. In fact, the functionality of a prism is to minimize the differences of optical path lengths [3], sharing the same principle with Scheimpflug condition. In other words, the purpose of using a prism may be fulfilled by reaching Scheimpflug condition. To prove that, we first go through the single camera calibration procedures for the case with a prism attached to a test section, as shown in Fig. 5(a). Laser pointers are placed and used to represent the respective object, lens, and image planes, aiding us in reaching Scheimpflug condition. For this case, the minimum calibration error we can get is 1.55 pixels. For the case without using a prism, as shown in Fig. 5(b), the minimum calibration error we can get is 0.84 pixel, i.e., even lower than that of the case using a prism. Finally, we set up a pair of cameras for a full SPIV calibration without using a prism. It is evident from the calibration images as shown in Fig. 6 that Scheimpflug condition is reached. In summary, the usage of a prism can be omitted if Scheimpflug condition is reached.

III. RESULTS

The resulting DP-SPIV system configuration is shown in Fig. 7. We use two LaVision Imager ProX 2M CCD cameras (maximum resolution: 1600 × 1200 pixels) as the SPIV camera pair. For the third camera, we use the VisionResearch Phantom v.310 High-Speed CMOS camera (maximum resolution at 3200 fps: 1280 × 800 pixels) because of its availability only. The laser used in this study is the Ekspla Nd:YAG double-cavity pulse laser, whose wave length is 532 nm (green) and maximum output is 180 mJ/pulse. The LaVision's software DaVis 7 is used for controlling image acquisition and then processing images to yield velocity vector maps. As explained in the previous section, the birefringent lens coupled with standard sheet-forming optics enables the generation of two parallel, orthogonally polarized light sheets with the separation distance (d) of 1 mm. In order for the cameras to image the designated light sheets, polarizing cube beam-splitters (Fig. 8) with orientations corresponding to designated polarizations of the light sheets are placed in front of the cameras.

Here we summarize the details of the system optimization and estimate their impacts on the reductions of item quantity, cost, and setup time in Table 2 and Table 3. Table 2 shows that Method A (birefringent optics) reduces the quantities of double-pulse laser and optics from 2 to 1 and 8 (from [16]) to 1, respectively; Method B (continuity equation) reduces the quantities of PIV camera from 4 to 3; Method C (Scheimpflug

Table 2. DP-SPIV system optimization estimation (item quantity).

Method	Item to be optimized	Result (Item quantity reduction)
(A) Birefringent optics	Double-Pulse Lasers	2 ➔ 1
	Optics	8 [16] ➔ 1
(B) Continuity Equation	PIV Cameras	4 ➔ 3
(C) Scheimpflug Condition	Prism & associated fixtures	1 ➔ 0

Table 3. DP-SPIV system optimization estimation (cost and setup time).

Method	Item to be optimized	Cost reduction (Approx.)	Setup time reduction (Approx.)
(A) Birefringent Optics	Double-Pulse Lasers	\$140 k ➔ \$70 k	36 hrs ➔ 6 hrs
	Optics	\$1 k ➔ \$0.4 k	
(B) Continuity Equation	PIV Cameras	\$120 k ➔ \$90 k	24 hrs ➔ 6 hrs
(C) Scheimpflug Condition	Prism & associated fixtures	\$0.2 k ➔ \$0 k	24 hrs ➔ 0 hrs
Total		\$261.2 k ➔ \$160.4 k	84 hrs ➔ 12 hrs

Note: **\$** = US Dollar

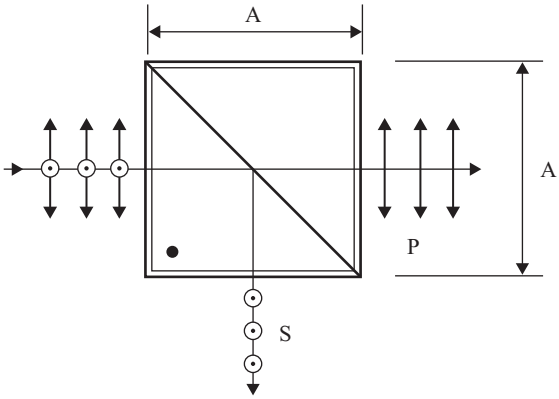

Fig. 8. Schematic of the polarizing cube beamsplitters [5].

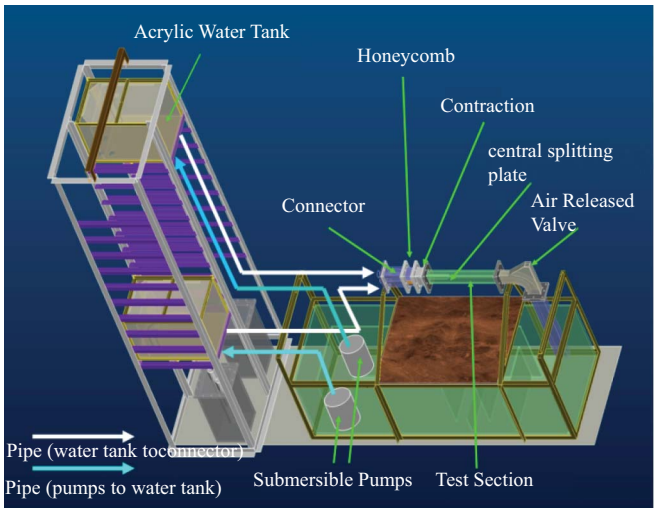

Fig. 9. Schematic of the shear-layer water tunnel.

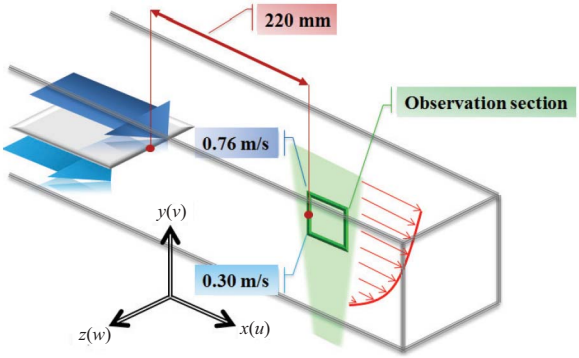

Fig. 10. Schematic of experimental conditions and parameters.

condition) replaces the functionality of a prism for this system and therefore no prism is needed. Table 3 estimates that, approximately, Method A (birefringent optics) contributes 70% and 42% to the total reductions of cost and setup time, respectively; Method B (continuity equation) contributes 29.8% and 25% to the total reductions of cost and setup time, respectively; Method C (Scheimpflug condition) contributes 0.2% and 33% to the total reductions of cost and setup time, respectively. It is obvious that birefringent optics is the most effective way in reducing both the cost and the setup time. It is interesting to see that Scheimpflug condition is not about reducing the cost (because the prism is much cheaper than the other items) but the setup time (1/3 of the total reduction). To conclude for this part, it is clearly evident that the optimized DP-SPIV system is much less complex and expensive, and much easier to build and set up.

We test the optimized DP-SPIV system and perform measurements in a shear-layer water tunnel as shown in Fig. 9. The upper and lower channels are separated with a flat plate whose end is made sharp to accommodate the merging of the two channel flows after it. The heights of the two water tanks can be independently adjusted according to the specific flow velocity gradients to be generated in the experiments. The cross-sectional area of the test section is 80 mm × 40 mm. The experimental conditions and parameters are shown in Fig. 10.

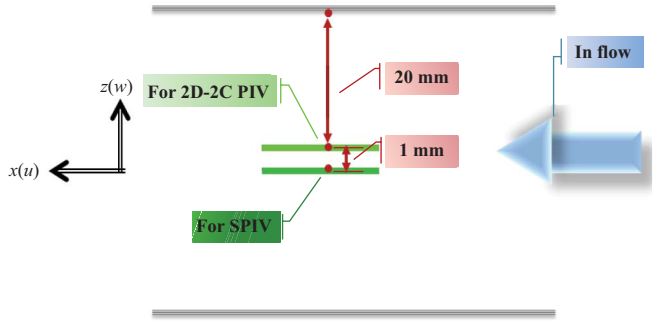

Fig. 11. Schematic of locations of the light sheets for the SPIV and 2D-2C PIV.

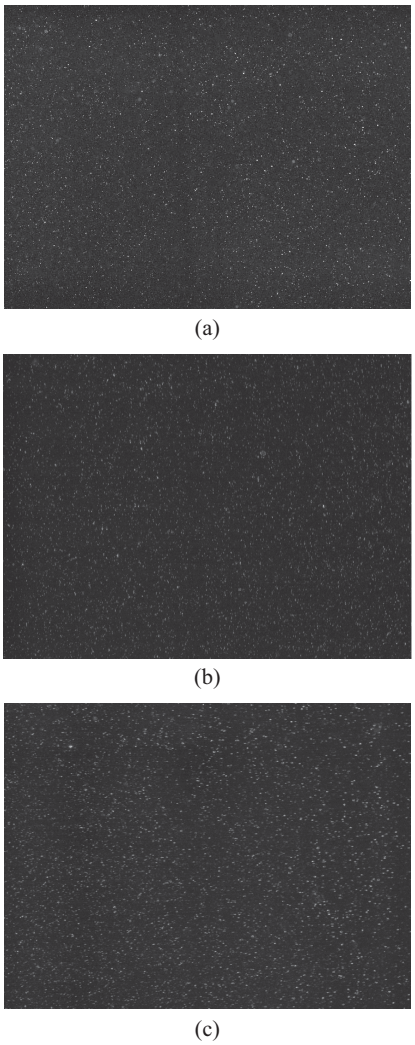

Fig. 12. Sample images acquired by (a) the high-speed camera, (b) the left camera of the SPIV pair, and (c) the right camera of the SPIV pair.

One of the two light sheets that is for SPIV measurement is aligned with the center plane of the tunnel, and the other light sheet is shifted 1 mm from the center plane as shown in Fig. 11. In order to match the image aspect ratio (4:3) of the CCD

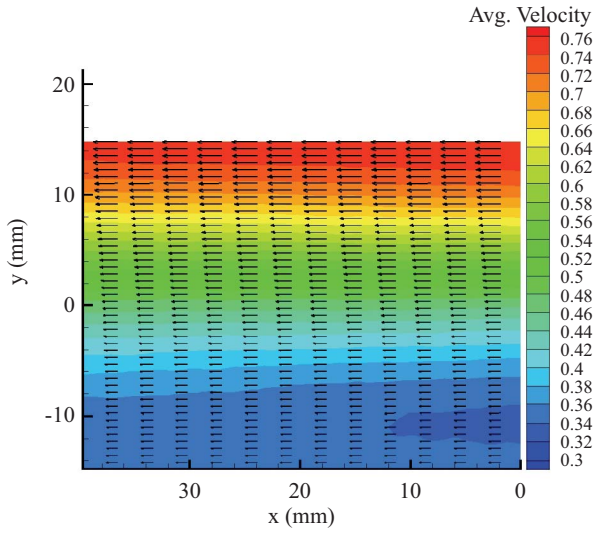

Fig. 13. Mean velocity vectors (u, v) and magnitude contours.

camera pair, we have to reduce the CMOS camera resolution down to 1024×768 pixels. Due to the physical pixel size of the CCD ($7.4 \times 7.4\ \mu m^2$) and the CMOS ($20 \times 20\ \mu m^2$) cameras are different, the magnifications for different cameras must be also adjusted accordingly. Eventually, the area of field of view is about 40 mm × 30 mm. The Reynolds number ($\Delta U \times h/\nu$) of this flow is about 4.0×10^4, where the characteristic length scale (height of the test section, h) is 80 mm, the characteristic velocity scale (ΔU = upper channel velocity − lower channel velocity) is about 0.50 m/s, and the kinematic viscosity (ν) of the water is 1.01×10^{-6}.

Figs. 12(a)~(c) show sample images of particles acquired in the experiment. It is clearly evident that these images are well in focus. The number of particles within a 64×64 pixels interrogation window can well reach 5~10, i.e., the rule of thumb about the number density of particles for PIV data analysis.

Two thousand image pairs are acquired for calculating mean variables. Fig. 13 shows the mean velocity vectors consisting of (u, v) components, with background contour plot showing the distribution of velocity magnitudes. The flow data of this figure clearly depict the structure of a shear-layer flow. Fig. 14 shows very small (relative to Fig. 13) mean w component contours, consistent with the fact that the flow is symmetric about the tunnel center plane. For examples of mean velocity gradients measured as shown in Figs. 15~17, $\partial w/\partial z$ calculated using Eq. (4) is almost zero as compared to the major shear $\partial u/\partial y$, also consistent with the flow symmetry. Theoretically, $\partial u/\partial z$ is also zero due to the flow symmetry. But actually, $\partial u/\partial z$ is obviously non-zero and relatively larger than other gradients except the major gradient $\partial u/\partial y$ (the explanations follows). Fig. 18 shows the distribution of turbulent kinetic energy (T.K.E.), and it is clearly evident that the value of T.K.E. peaks in the range of y = 0~10 mm. Fig. 19 shows the distribution of turbulence production (p) defined as

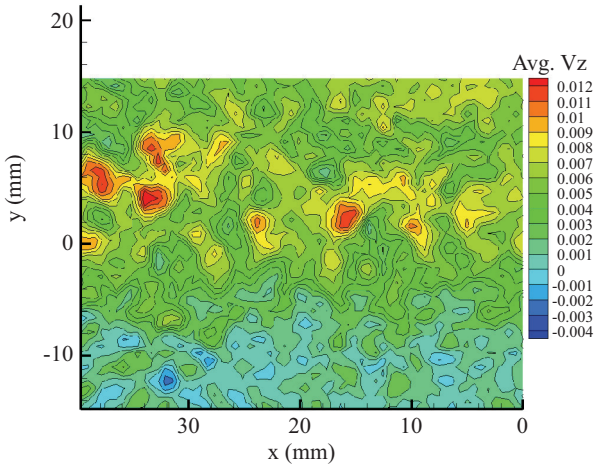

Fig. 14. Mean *w* component contours.

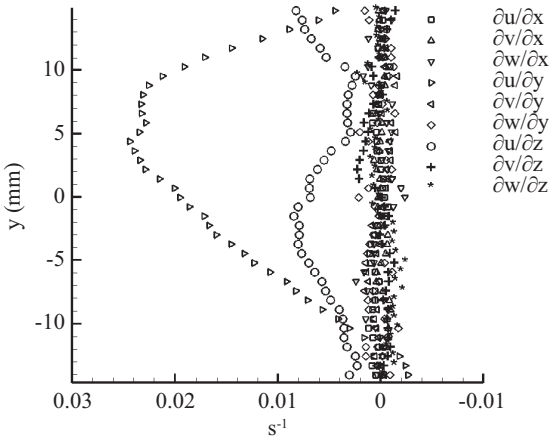

Fig. 17. All mean velocity gradient at *x* = 30 mm.

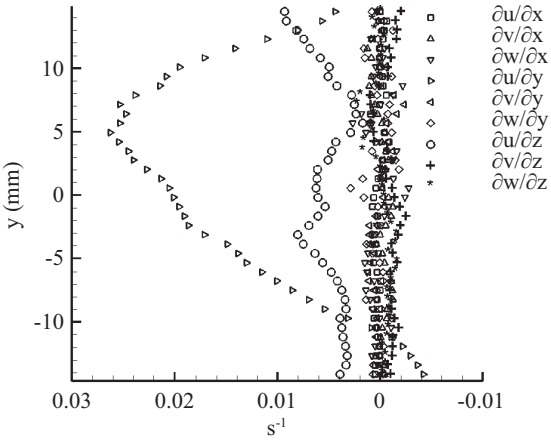

Fig. 15. All mean velocity gradients at *x* = 10 mm.

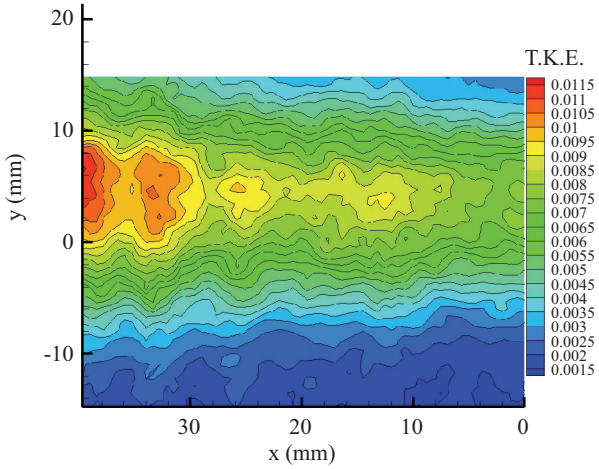

Fig. 18. Contour of turbulence kinetic energy.

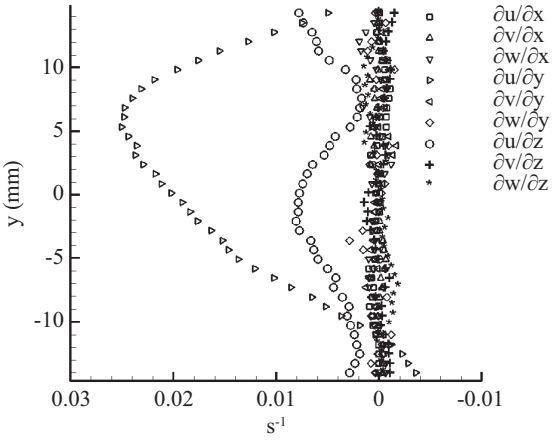

Fig. 16. All mean velocity gradients at *x* = 20 mm.

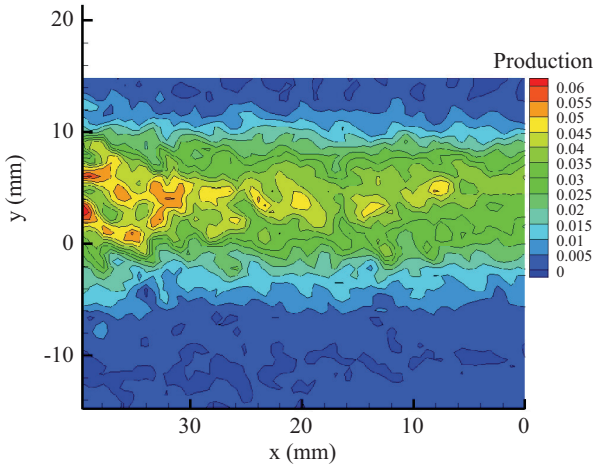

Fig. 19. Contour of total rate turbulence production of T.K.E.

$$p = -\overline{u_i' u_j'} \frac{\partial \overline{u}_i}{\partial x_j} \quad (5)$$

Obviously, the peak locations of both T.K.E. and turbulence production are quite matched. This fact becomes more clearly evident as shown in Figs. 20(a)~(c), where the peak locations can be pinpointed at about $y = 5$ mm. This result also indicates that our measurement is consistent with the physical fact

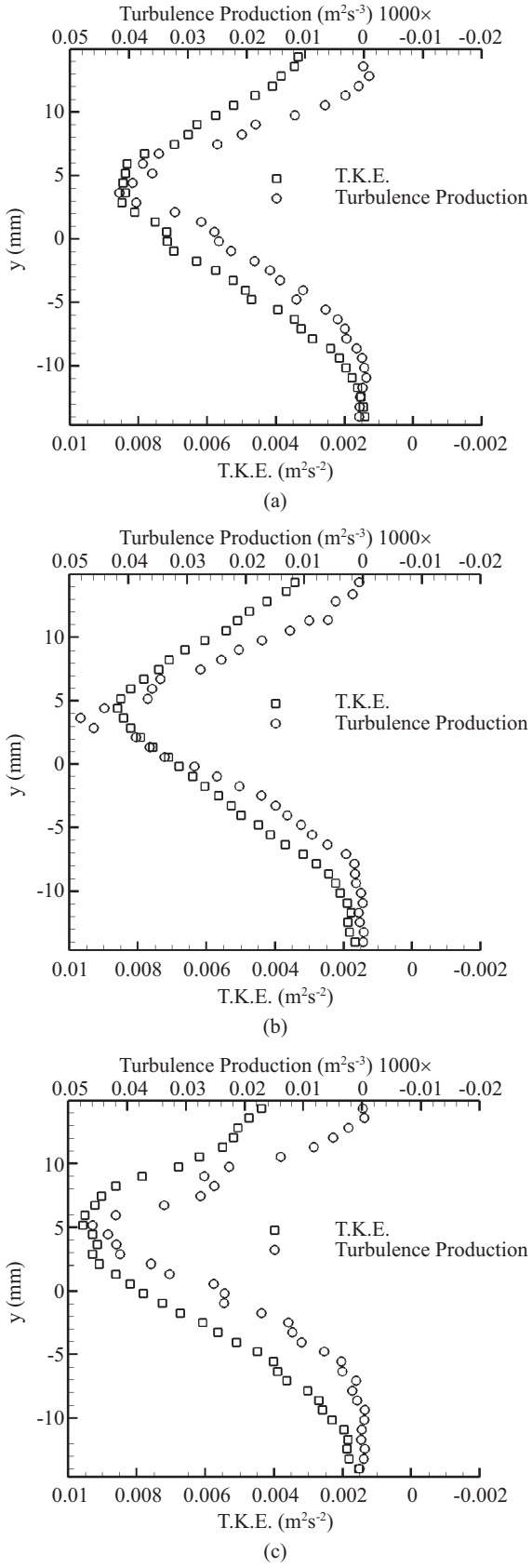

Fig. 20. Turbulence kinetic energy and turbulence production at (a) x = 10 mm, (b) 20 mm, and (c) 30 mm.

inherent in this flow, i.e., the peaking turbulence production generates the highest T.K.E.

IV. UNCERTAINTY AND DEVIATION ANALYSIS

In our SPIV system, we perform evaluations of position deviation, image reconstructions, and self-calibrations using a calibration target board and software provided by LaVision ([8]). After the full calibration procedures, the average position uncertainty calculated by the software is 1.26 pixels.

The second uncertainty source comes from the cross-correlation procedure. We have used some synthesized images to test LaVision's Flow Master, the cross-correlation engine we use in our measurement, and estimated the average uncertainty associated with this procedure to be 0.40 pixel.

Since the whole analysis procedures consist of two cross-correlation calculations each of which is for image pairs from the left or right camera, and one calibration step, the combined uncertainty $\varepsilon_{\Delta x}$ for the particle displacement (flow velocity) can be estimated as

$$\varepsilon_{\Delta x} = (1.26^2 + 2\times 0.4^2)^{0.5}$$
$$\approx 1.38 \text{ (pixel)} \tag{6}$$

Since we acquire 2000 realizations for calculating mean variables, this averaging procedure may further reduce the uncertainty by $1/(2000)^{0.5}$ assuming all the errors are random processes. For example, the uncertainty associated with the mean particle displacement can be estimated as $1.38/(2000)^{0.5} = 0.03$ pixel. Therefore, for a typical mean particle displacement of 10 pixels, the relative uncertainty can be estimated as 0.03/10 = 0.3%.

To estimate the measurement deviations associated with velocity gradients for this system, one may use the symmetry inherent in this flow. Due to the symmetry, the theoretical value of mean w velocity component and the mean velocity gradients in z direction on the center plane ($z = 0$) must be zero. Therefore,

$$\frac{\partial w}{\partial x} = \frac{\partial w}{\partial y} = \frac{\partial u}{\partial z} = \frac{\partial v}{\partial z} = \frac{\partial w}{\partial z} = 0 \tag{7}$$

by defining K as

$$K = \left| \left(gradient\right)_{exp.} - \left(gradient\right)_{theory} \right| \tag{8}$$

it can be readily seen that K is equal to the absolute individual deviation for these five velocity gradients. In order to estimate their relative deviations from the gradient tensor as a whole, we need to first estimate the magnitude (G) of the gradient tensor as follows

$$G=\left[\begin{array}{l}\left(\frac{\partial u}{\partial x}\right)^2+\left(\frac{\partial v}{\partial x}\right)^2+\left(\frac{\partial w}{\partial x}\right)^2+\left(\frac{\partial u}{\partial y}\right)^2+\left(\frac{\partial v}{\partial y}\right)^2 \\ +\left(\frac{\partial w}{\partial y}\right)^2+\left(\frac{\partial u}{\partial z}\right)^2+\left(\frac{\partial v}{\partial z}\right)^2+\left(\frac{\partial w}{\partial z}\right)^2\end{array}\right]^{\frac{1}{2}} \quad (9)$$

by substituting Eq. (7) into Eq. (9), we can obtain

$$G=\left[\left(\frac{\partial u}{\partial x}\right)^2+\left(\frac{\partial v}{\partial x}\right)^2+\left(\frac{\partial u}{\partial y}\right)^2+\left(\frac{\partial v}{\partial y}\right)^2\right]^{\frac{1}{2}} \quad (10)$$

Finally, by evaluating the ratio *K/G* we may estimate the relative deviations associated with these five velocity gradients. Figs. 21~23 show the relative deviations of the five gradient $\partial w/\partial x$, $\partial w/\partial y$, $\partial u/\partial z$, $\partial v/\partial z$, and $\partial w/\partial z$ at x = 10 mm, 20 mm, and 30 mm, respectively. The deviations of the gradients $\partial w/\partial x$ and $\partial w/\partial y$ are mostly less than 1% due to the fact that the w velocity component is much lower than the dominating u component. Deviations of the other three gradients are much higher and even more than 100% at the top and bottom areas. It is due to the fact that G is almost zero near the top and bottom areas, i.e., uniform flows without significant velocity gradients. Among them, $\partial u/\partial z$ exhibits the largest deviation mainly due to the large light sheet separation (d = 1 mm). It can be improved by replacing the current birefringent lens with one that has a shorter walk-off distance. However, the overlapping volume of the two light sheets increases with reducing their separation distance, resulting in reduction of statistical relevancy of the finite difference scheme for evaluating ∂u. The optimal overlapping ratio would be 50%, which translates to 0.5 mm center-to-center distance of the two 1 mm thick light sheets in our case. It is quite easy to acquire such a birefringent lens product with 0.5 mm walk-off distance at a similar price. Therefore, the cost raised due to this improvement is minimum and may even be zero. Table 4 shows the average relative deviations of the five velocity gradients within the area of measurement. For $\partial u/\partial x$, $\partial u/\partial y$, $\partial v/\partial x$, and $\partial v/\partial y$, there are no such theoretical values for us to estimate their deviations. They are, however, in-plane variables as opposed to out-of-plane ones such as $\partial u/\partial z$. Therefore, the relative deviations of these four velocity gradients are expected to be much less than that of $\partial u/\partial z$ and around that of $\partial v/\partial z$ and $\partial w/\partial z$.

V. CONCLUSION

A cost-effective DP-SPIV system has been proposed and successfully developed. As summarized in Tables 2 and 3, the optimized system is estimated to reduce the cost to nearly one half of and the setup time to almost one order of magnitude shorter than that of the conventional configuration. Birefringent optics turns out to be the most effective way in optimizing the system.

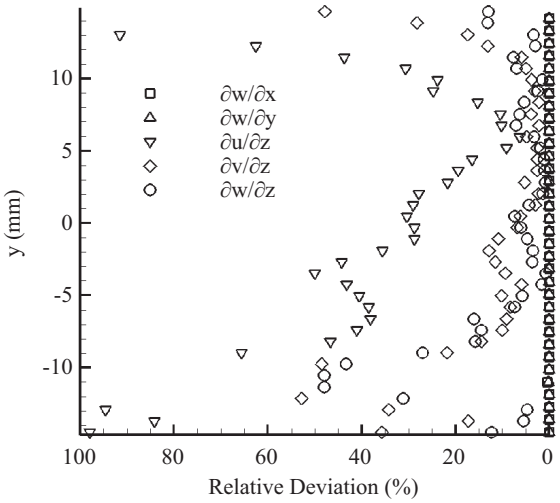

Fig. 21. Relative deviations in five gradients at x = 10 mm.

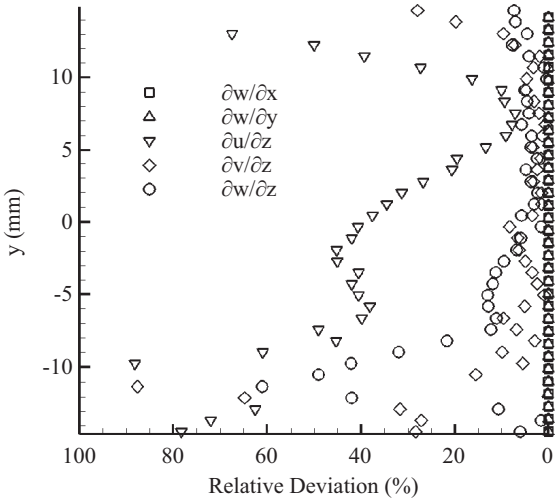

Fig. 22. Relative deviations in five gradients at x = 20 mm.

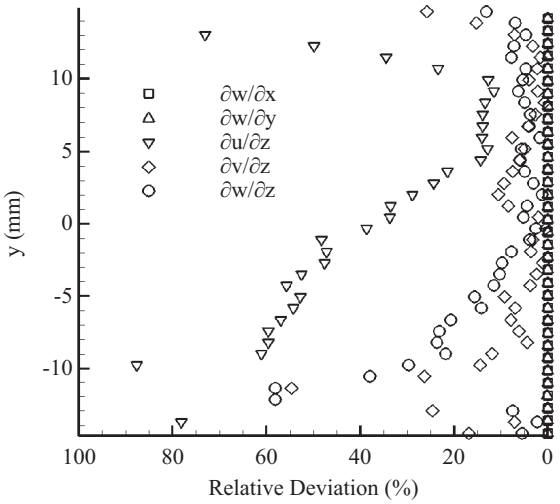

Fig. 23. Relative deviations in five gradients at x = 30 mm.

Table 4. Mean relative deviations in five velocity gradients.

K	K/G (%)
$\partial w/\partial x$	0.016
$\partial w/\partial y$	0.016
$\partial u/\partial z$	64.71
$\partial v/\partial z$	14.22
$\partial w/\partial z$	11.76

Using the simple, shear-layer flow experiment, we verify that this DP-SPIV system works for the measurement of turbulent flows. Future works include using this measurement system to investigate some highly complicated turbulent flows such as marine propeller flows, and addressing issues of associated turbulence modeling.

REFERENCES

1. Elsinga, G. E., Scarano, F., Wieneke, B., and van Oudheusden, B. W., "Tomographic particle image velocimetry," *Experiments in Fluids*, Vol. 41, pp. 933-947 (2006).
2. Ganapathisubramani, B., Longmire, E. K., Marusic, I., and Pothos, S., "Dual-plane PIV technique to determine the complete velocity gradient tensor in a turbulent boundary layer," *Experiments in Fluids*, Vol. 39, pp. 222-231 (2005).
3. Hecht, E., *Optics*, Addison Wesley (2002).
4. Hinze, J. O., *Turbulence*, McGraw-Hill Publishing Co., New York (1975).
5. LAMBDA Research Optics, Inc., http://www.lambda.cc/index.php.
6. Launder, B. E., Reece, G. J., and Rodi, W., "Progress in the development of a Reynolds-stress turbulence closure," *Journal of Fluid Mechanics*, Vol. 68, No. 3, pp. 537-566 (1975).
7. Launder, B. E. and Spalding, D. B., *Lectures in Mathematical Models of Turbulence*, Academic Press, London, England (1972).
8. LaVision System DaVis 7 Manual (2007).
9. Pereira, F. and Gharib, M., "Defocusing digital particle image velocimetry and the three-dimensional characterization of two-phase flows," *Measurement Science and Technology*, Vol. 13, pp. 683-694 (2002).
10. Prasad, A. K., "Stereoscopic particle image velocimetry," *Experiments in Fluids*, Vol. 29, pp. 103-116 (2000).
11. Raffel, M., Willert, C. E., and Kompenhans, J., *Particle Image Velocimetry*, Springer, Berlin (1998).
12. Reynolds, W. C., "The potential and limitations of direct and large eddy simulations," in: Lumley, J. L. (Ed.), *Whither Turbulence? Turbulence at the Crossroads*, Springer-Verlag, Berlin, pp. 313-343 (1990).
13. Saikrishnan, N., Marusic, I., and Longmire, E. K., "Assessment of dual plane PIV measurements in wall turbulence using DNS data," *Experiments in Fluids*, Vol. 41, pp. 265-278 (2006).
14. Scheimpflug, T., "Improved method and apparatus for the systematic alteration or distortion of plane pictures and images by means of lenses and mirrors for photography and for other purposes," GB Patent No. 1196 (1904).
15. Smagorinsky, J., "General circulation experiments with the primitive equations: I. the basic experiment, " *Monthly Weather Review*, Vol. 91, pp. 99-164 (1963).
16. Tanahashi, M., Hirayama, T., Ueda, T., and Miyauchi, T., "Parallel beam forming optics for the reduction of laser requirements in dual-plane stereoscopic PIV," *14th International Symposium on Applications of Laser Techniques to Fluid Mechanics*, Lisbon, Portugal (2008).
17. Wilcox, D. C., *Turbulence Modeling for CFD*, DCW Industries, Inc., La Canada, California (1998).
18. Zhang, J., Tao, B., and Katz, J., "Turbulent flow measurement in a square duct with hybrid holographic PIV," *Experiments in Fluids*, Vol. 23, pp. 373-381 (1997).